

THE ORBITAL ANGULAR MOMENTUM OF LIGHT

by

Nicholas Paul Pellatz

A thesis submitted in partial fulfillment of the requirements  
for graduation with Honors in Physics.

Whitman College  
2014

*Certificate of Approval*

This is to certify that the accompanying thesis by Nicholas Paul Pellatz has been accepted in partial fulfillment of the requirements for graduation with Honors in Physics.

---

Mark Beck, Ph.D.

Whitman College  
May 15, 2014

# Contents

<b>1</b>	<b>Introduction</b>	<b>1</b>
<b>2</b>	<b>Theory</b>	<b>5</b>
2.1	Orbital Angular Momentum in Paraxial Beams . . . . .	5
2.2	Generation of the LG Modes . . . . .	8
2.3	Interference of the LG Modes . . . . .	11
<b>3</b>	<b>Experiment</b>	<b>14</b>
3.1	Table Setup for Generating and Interfering LG Modes . . . . .	14
3.2	Generating Single LG Modes . . . . .	16
3.3	Superpositions of LG Modes . . . . .	21
3.4	Sorting Even and Odd LG Modes . . . . .	24
<b>4</b>	<b>Conclusion</b>	<b>28</b>
<b>A</b>	<b>Detailed Experimental Setup</b>	<b>30</b>
<b>B</b>	<b><i>LabVIEW</i> Programming</b>	<b>32</b>

# Abstract

Here we present the results of an exploration of the Laguerre-Gaussian (LG) modes of laser light. These modes, each characterized by an integral index  $l$ , carry orbital angular momentum due to their helical phase fronts. We demonstrate methods of generating the LG modes from a simple Gaussian mode using computer-generated holograms and find that we can generate each of the LG modes with indices  $l = -3$  through  $l = 3$ . We also predict and confirm the behavior of positive and negative LG modes in a superposition. The intensity pattern of a superposition of an LG mode with index  $l$  and one with index  $-l$  is a symmetric arrangement of  $2l$  bright spots which rotate as the relative phase between the two beams is adjusted. Finally, we explore an interferometric method of sorting even and odd modes from a superposition and find that we can separate an  $l = 0$  mode and an  $l = 1$  mode from a superposition of the two.

# List of Figures

1.1	The intensity profile of a simple Gaussian mode. . . . .	1
1.2	The intensity profile of an $l = 1$ LG mode. . . . .	2
1.3	An $l = 1$ forked diffraction grating. . . . .	3
2.1	Simplified depiction of how a hologram works. . . . .	9
2.2	Simulated interference of tilted LG beam and Gaussian reference beam.	11
2.3	Starting on the left and going right, $l = -1, +2$ , and $+3$ holograms. .	11
2.4	Starting top-left and going clockwise, interference patterns for $l_1 - l_2 = 2, 4$ , and $6$ ( $\delta = 0$ ). . . . .	13
2.5	Intensity patterns for $l_1 - l_2 = 2$ with $\delta = \pi/2$ and $\delta = \pi$ . . . . .	13
3.1	Modified Sagnac interferometer used to form superpositions of LG modes.	15
3.2	In the top-left, a photograph of the first diffracted beam using an $l = 1$ hologram. This photograph is $300 \times 300$ pixels with an exposure time of 10ms. In the bottom left, the intensity of each pixel from the image above plotted vertically. The top-right and bottom-right images are theoretical fits of the data on the left to Equation 3.1. . . . .	17
3.3	In the top-left, a photograph of the first diffracted beam using an $l = 2$ hologram. This photograph is $360 \times 360$ pixels with an exposure time of 10ms. In the bottom left, the intensity of each pixel from the image above plotted vertically. The top-right and bottom-right images are theoretical fits of the data on the left to Equation 3.1. . . . .	19

3.4 On the left, a photograph of the first diffracted beam using an $l = 3$ hologram. This photograph is $400 \times 400$ pixels with an exposure time of 10ms. On the right, a theoretical fit of the data to Equation 3.1. . . . .	20
3.5 Starting on the left and going right, first-order diffracted beams for $l = 1$ , $l = 2$ , and $l = 3$ holograms shown on the same scale (each photograph had an exposure time of 10ms and was cropped to $360 \times 360$ pixels). . . . .	20
3.6 In the top row, theoretical intensity patterns for the superpositions of LG modes labeled above. Subsequent rows show photographs of superpositions with each row having slightly more relative phase between the interfering beams than the row above. Here, each photograph had an exposure time of 10ms and was cropped to $320 \times 320$ pixels. . . . .	23
3.7 An illustration of the way a Dove prism flips a laser beam over the axis defined by it's lower base. . . . .	24
3.8 Altered version of the interferometer in Figure 3.1 with Dove prisms in each arm. The Dove prisms are oriented at $90^\circ$ with respect to each other for sorting odd and even LG modes. . . . .	25
3.9 Illustration of what happens to even and odd modes in the two arms of our sorting interferometer. . . . .	26
3.10 Photographs of the two outputs of the sorting interferometer when the input is a superposition of $l = 0$ and $l = 1$ states. Each photograph has a slight increase in the relative phase $\delta$ from the one above it. If the top photograph has $\delta = 0$ , then the third photograph has $\delta = \pi$ , and the final photograph has $\delta = 2\pi$ . The photographs all have resolution $1260 \times 460$ pixels and were taken with an exposure time of 50 ms. . . . .	27
A.1 Photograph of our table setup including both the generating interferometer and the sorting interferometer. . . . .	30
A.2 Detailed diagram of the table setup shown in Figure A.1. . . . .	31

B.1	Block diagram for WindSettings.vi which sets parameters for one window.	32
B.2	Front panel for Open External Window.vi. . . . .	33
B.3	Block diagram for Open External Window.vi. . . . .	34
B.4	Basler program used to capture photographs with the USB camera used in the lab. . . . .	35

# Chapter 1

## Introduction

Without thinking, it is easy to make the mistake of assuming that the output of a laser is a uniform column of light. The more complicated truth is that the output of any laser, being comprised of electromagnetic waves, must satisfy Maxwell's equations. This condition on a laser beam restricts the possible light output to a number of various modes. For instance, the output of a typical laser is in the Gaussian mode. A laser in the Gaussian mode shining on a screen is brightest in the middle and gets dimmer further from the center as can be seen in Figure 1.1. In fact, the intensity profile across any diameter of the beam follows the familiar Gaussian "bell curve" shape. Of course there are many other modes which a beam of laser light can be in and many ways of transforming a beam in the Gaussian mode to another mode.

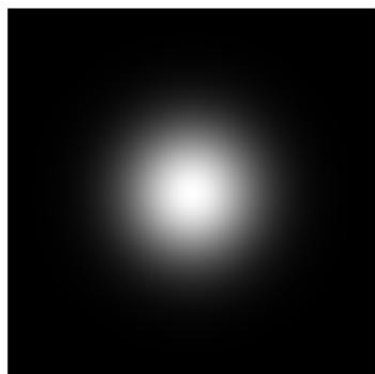


Figure 1.1: The intensity profile of a simple Gaussian mode.

In this study, we were most interested in the set of modes known as the Laguerre-Gaussian (LG) modes. The electric field of the LG modes is characterized by two indices, usually  $p$  and  $l$ . Here we restrict ourselves to an investigation of the subset of the LG modes whose  $p$  index is 0. The index  $l$  can then take on any integer value. The intensity profile of the LG mode with  $l = 1$  is shown in Figure 1.2. This intensity profile, however, hides the more complicated structure of the LG modes. Recall that the Poynting vector characterizes the direction and magnitude of energy flow for electromagnetic waves. In a simple Gaussian beam, the Poynting vector points straight along the beam axis. In the LG modes on the other hand, the Poynting vector moves in a spiral about the beam axis as the beam propagates [1]. The value of the index  $l$  characterizes the tightness of the Poynting vector's spiral.

There are several different methods for creating a beam in an LG mode. One method involves putting the laser beam through two  $\pi/2$  mode converters. This method, however, requires the input to be in one of the Hermite-Gaussian modes. Each Hermite-Gaussian mode gets converted into a different LG mode [1]. The method preferred in this study is one that uses a Spacial Light Modulator (SLM) to get a variety of LG modes from a single Gaussian beam. An SLM has a liquid crystal display which allows the creation of any diffraction grating needed. This technology is widely used in commercial LCD projectors [2]. On the SLM, we place a

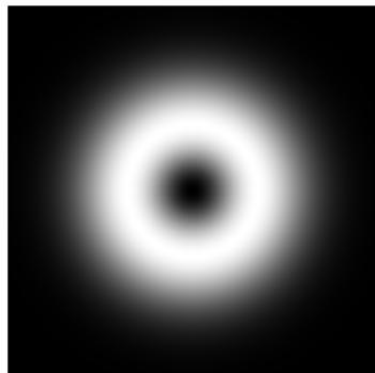


Figure 1.2: The intensity profile of an  $l = 1$  LG mode.

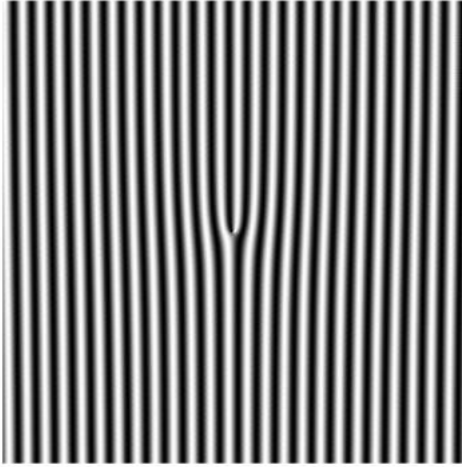


Figure 1.3: An  $l = 1$  forked diffraction grating.

special forked diffraction grating, an example of which is illustrated in Figure 1.3. The grating shown is an  $l = 1$  grating, which means that the first order diffracted beam when this grating is illuminated with a Gaussian beam will be the  $l = 1$  LG mode. In fact, the  $m$ th order diffracted beam will be in the  $l = m$  LG mode. The mathematical origins of these forked gratings will be explored further in Chapter 2.

What is perhaps most surprising about the LG modes is that they carry orbital angular momentum. A beam of light in the LG mode with index  $l$  carries orbital angular momentum equal to  $l\hbar$  per photon, and because  $l$  can only take on integer values the orbital angular momentum is quantized [3]. We will motivate these assertions in Section 2.1. The fact that  $l$  can only take on integer values follows from an exponential  $e^{il\phi}$  term in the electric field amplitude of the LG modes (here,  $\phi$  is the angle in the plane perpendicular to the beam axis). As we should expect, this term oscillates about the beam axis with a frequency dependent on  $l$ . Of course, if  $\phi$  is increased by  $2\pi$ , then the field should be the same. In other words,  $e^{il\phi} = e^{il(\phi+2\pi)} = e^{il\phi}e^{il2\pi}$ . But  $e^{il2\pi}$  will equal 1 only if  $l$  is an integer. Thus, the orbital angular momentum is quantized for beams with  $\phi$  dependence  $e^{il\phi}$ .

The orbital angular momentum variable exhibits quantum properties very similar to those of the spin variable for photons. It has been shown experimentally that

pairs of photons can be entangled in their orbital angular momentum [4]. There has even been a demonstration of an indeterminacy relation between the angular position of a photon in a beam and its orbital angular momentum [5]. What sets orbital angular momentum apart from spin angular momentum, however, is the fact that for photons there are only two spin states available, but infinitely many orbital angular momentum states. The variable  $l$  can take on any integer value. We also have good classical reasons to believe that the quantum states corresponding to the LG modes form a complete and orthogonal basis set [3]. In other words, the orbital angular momentum state of any photon can be written as a linear combination of LG states and none of the LG states themselves can be written as a linear combination of any other LG states. For this reason, we say that the LG states define an infinite-dimensional Hilbert space.

The study of the quantum properties of the LG states is still relatively young (the first demonstration of entanglement in the orbital angular momentum variable was as recent as 2001 [4]). The infinite-dimensional nature of the LG state space makes it a potentially very fruitful space in which to study entanglement effects and try to understand them on a deeper level. But in order to perform entanglement experiments, we must first have a solid understanding of how the LG modes can be generated, superimposed, and sorted efficiently. The research presented here represents an important step towards being able to study entanglement of orbital angular momentum states in an undergraduate laboratory.

# Chapter 2

## Theory

### 2.1 Orbital Angular Momentum in Paraxial Beams

It is instructive to first see how light beams treated classically can carry orbital angular momentum. The work within this section will all be done within the approximation that the transverse spatial distribution of the beam of light does not vary rapidly as the beam propagates (known as the paraxial approximation). Let  $u(x, y, z)$  be the spatial amplitude distribution for our beam of light and let the beam axis lie along  $\hat{\mathbf{z}}$ . We will then take our vector potential to be oriented along the  $x$ -axis:

$$\mathbf{A} = u(x, y, z) e^{i(kz - \omega t)} \hat{\mathbf{x}}$$

Here,  $k$  is the wave vector and  $\omega$  is the angular frequency. The magnetic field is then

$$\mathbf{B} = \nabla \times \mathbf{A} = ik \left[ \left( u - \frac{i}{k} \frac{\partial u}{\partial z} \right) \hat{\mathbf{y}} + \frac{i}{k} \frac{\partial u}{\partial y} \hat{\mathbf{z}} \right] e^{i(kz - \omega t)}.$$

Within the paraxial approximation, however,  $ku$  is much greater than  $\frac{\partial u}{\partial z}$  in magnitude. In that case, the magnetic field becomes

$$\mathbf{B} \approx ik \left[ u \hat{\mathbf{y}} + \frac{i}{k} \frac{\partial u}{\partial y} \hat{\mathbf{z}} \right] e^{i(kz - \omega t)}. \quad (2.1)$$

Now, according to Maxwell's equations, the electric field  $\mathbf{E}$  has dependence on both the time derivative of  $\mathbf{A}$  and the spatial derivative of the scalar potential  $V$ . So the

next thing to do is choose a gauge to work within and find the scalar potential  $V$  in that gauge. In the Lorentz gauge, the relationship between the vector and scalar potentials is given by [6]

$$\nabla \cdot \mathbf{A} = -\frac{1}{c^2} \frac{\partial V}{\partial t}.$$

Plugging in our expression for  $\mathbf{A}$  and solving for  $V$ , we find that

$$\frac{\partial u}{\partial x} e^{i(kz-\omega t)} = \frac{-1}{c^2} \frac{\partial V}{\partial t} \implies V = \frac{c^2}{i\omega} e^{i(kz-\omega t)} \frac{\partial u}{\partial x} = \frac{\partial}{\partial x} \left[ \frac{c^2}{i\omega} u e^{i(kz-\omega t)} \right].$$

Then, knowing  $\mathbf{A}$  and  $V$ , the electric field is

$$\begin{aligned} \mathbf{E} &= -\nabla V - \frac{\partial A}{\partial t} = -\frac{c^2}{i\omega} \nabla \left[ \frac{\partial}{\partial x} (u e^{i(kz-\omega t)}) \right] + i\omega u e^{i(kz-\omega t)} \\ &= -\frac{c^2}{i\omega} \frac{\partial}{\partial x} [u \nabla e^{i(kz-\omega t)} + e^{i(kz-\omega t)} \nabla u] + i\omega u e^{i(kz-\omega t)} \end{aligned} \quad (2.2)$$

I have written out the gradient of  $V$  in this way in order to make the observation that  $u$  changes on length scales much longer than a wavelength while  $e^{i(kz-\omega t)}$  oscillates quickly on the order of a wavelength. Therefore, the first term in brackets in Eqn. 2.2 is much larger than the second term. Throwing out the second term, we are left with an expression for  $\mathbf{E}$  which is similar in form to Eqn. 2.1:

$$\mathbf{E} \approx ikc \left[ u \hat{\mathbf{x}} + \frac{i}{k} \frac{\partial u}{\partial x} \hat{\mathbf{z}} \right] e^{i(kz-\omega t)}$$

We have now described both the magnetic and electric fields of our beam without assuming anything about the form of  $u(x, y, z)$  other than the fact that the beam is paraxial. A natural next step to take would be to calculate the Poynting vector for this beam since the Poynting vector contains information about the beam's momentum and energy.

According to Griffiths, the Poynting vector is the energy flux density, or energy per unit time per unit area, in an electromagnetic field [6]. It's time-averaged form is given by

$$\langle \mathbf{S} \rangle = \frac{1}{\mu_0} \langle \mathbf{E} \times \mathbf{B} \rangle = \frac{1}{2\mu_0} (\mathbf{E}^* \times \mathbf{B} + \mathbf{E} \times \mathbf{B}^*).$$

If we then plug in our expressions for  $\mathbf{E}$  and  $\mathbf{B}$ , we find that

$$\langle \mathbf{S} \rangle = \frac{ikc}{2\mu_0} \left[ \left( u \frac{\partial u^*}{\partial x} - u^* \frac{\partial u}{\partial x} \right) \hat{\mathbf{x}} + \left( u \frac{\partial u^*}{\partial y} - u^* \frac{\partial u}{\partial y} \right) \hat{\mathbf{y}} \right] + \frac{k^2 c}{\mu_0} |u|^2 \hat{\mathbf{z}}.$$

This equation takes a slightly simpler form if we define a gradient-like operator  $\hat{O} \equiv (\frac{\partial}{\partial x} \hat{\mathbf{x}} + \frac{\partial}{\partial y} \hat{\mathbf{y}})$ :

$$\langle \mathbf{S} \rangle = \frac{ikc}{2\mu_0} \left( u \hat{O} u^* - u^* \hat{O} u \right) + \frac{k^2 c}{\mu_0} |u|^2 \hat{\mathbf{z}}. \quad (2.3)$$

Up to this point, we have been working completely within Cartesian coordinates even though cylindrical coordinates are the more natural choice if we want to think about angular momentum along the  $z$ -axis. Equation 2.3 lets us transform to cylindrical coordinates by rewriting our defined operator:

$$\hat{O} \equiv \left( \frac{\partial}{\partial x} \hat{\mathbf{x}} + \frac{\partial}{\partial y} \hat{\mathbf{y}} \right) = \left( \frac{\partial}{\partial r} \hat{\mathbf{r}} + \frac{1}{r} \frac{\partial}{\partial \phi} \hat{\phi} \right).$$

We now assume that  $u(x, y, z)$  can be written as

$$u(x, y, z) = u(r, \phi, z) = u_0(r, z) e^{il\phi}. \quad (2.4)$$

In general,  $l$  could be any complex number. But since  $u(r, \phi, z)$  is a physical quantity, it must be single-valued. In other words, we must have

$$u(r, \phi, z) = u(r, \phi + 2\pi, z) \implies u_0(r, z) e^{il\phi} = u_0(r, z) e^{il\phi} e^{il2\pi} \implies e^{il2\pi} = 1.$$

This means that  $l$  must be an integer. We can then find the  $\phi$  component of our expression for the Poynting vector:

$$\begin{aligned} \langle \mathbf{S} \rangle_\phi &= \frac{ikc}{2\mu_0} \left( u_0 e^{il\phi} \frac{1}{r} \frac{\partial}{\partial \phi} (u_0^* e^{-il\phi}) - u_0^* e^{-il\phi} \frac{1}{r} \frac{\partial}{\partial \phi} (u_0 e^{il\phi}) \right) \\ &= \frac{l k c |u|^2}{\mu_0 r} \end{aligned} \quad (2.5)$$

The spatial amplitude distribution for the LG modes can, in fact, be written in the form of Equation 2.4. This calculation will then show that *any* beam of light whose azimuthal dependence is  $e^{il\phi}$  carries orbital angular momentum. What we have in Eqn. 2.5 is the energy flux density in the  $\hat{\phi}$  direction. To get the momentum in

that direction, we simply divide by  $c$ . The angular momentum flux density along the  $z$ -axis then, is the cross product of  $\mathbf{r}$  with  $\langle \mathbf{S} \rangle_\phi / c$ :

$$L_z \hat{\mathbf{z}} = \mathbf{r} \times \left( \frac{lkc|u|^2}{\mu_0 r} \hat{\phi} \right) = \frac{lk|u|^2}{\mu_0} \hat{\mathbf{z}}$$

We now clearly see that the beam carries an amount of angular momentum along the  $z$  axis. To get a better sense of just how much angular momentum is carried, we can compare  $L_z$  to the energy flux density carried by the beam along its  $z$  axis:

$$\langle \mathbf{S} \rangle_z = \frac{k^2 c}{\mu_0} |u|^2$$

So, the ratio of angular momentum to energy along the axis of propagation is

$$\frac{L_z}{\langle \mathbf{S} \rangle_z} = \frac{l}{ck} = \frac{l}{\omega} \quad (2.6)$$

In other words, the ratio of angular momentum to energy in a beam with the  $\phi$ -dependence of Equation 2.4 is just the index  $l$  over the frequency. This result is very suggestive since multiplying the numerator and denominator by  $\hbar$  gives the familiar form  $\hbar\omega$  in the denominator, which is interpreted quantum mechanically as the energy per photon in the beam. This motivates the belief that individual photons carry an amount  $l\hbar$  of orbital angular momentum. The treatment up to Equation 2.6, however, has been wholly classical, so it would be a mistake to take this as a rigorous proof of the amount of orbital angular momentum carried by photons.

## 2.2 Generation of the LG Modes

In order to understand how the forked diffraction gratings described in Chapter 1 can convert a Gaussian laser beam to a Laguerre-Gaussian one, it is first necessary to understand a few basic principles of holography. In a general sense, a hologram is like a photograph in that it is a way of storing optical information. Unlike a photograph, however, a hologram stores information about both the intensity and the phase of

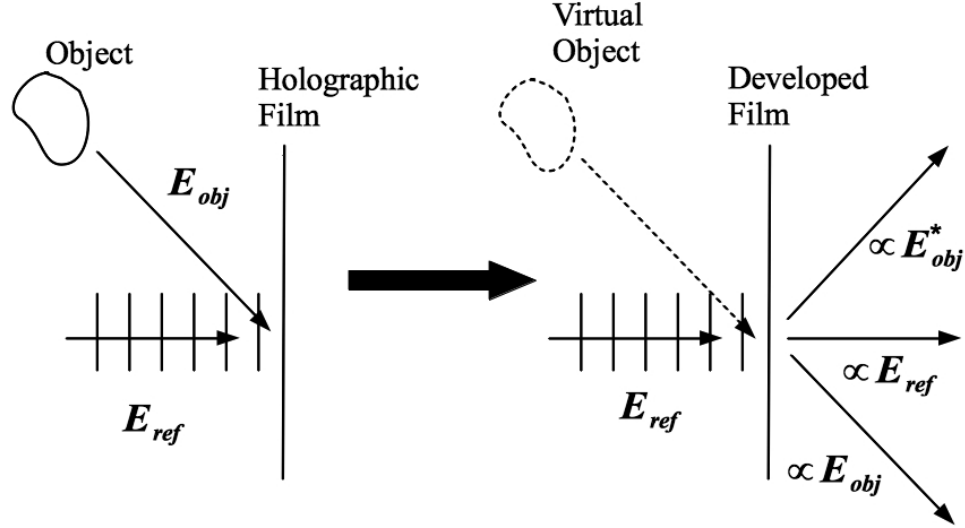


Figure 2.1: Simplified depiction of how a hologram works.

the field of the object. A basic diagram of how a hologram works is offered in Figure 2.1.

When the hologram is being formed, we interfere a reference beam (depicted as a plane wave in Figure 2.1) with the light from the object we are trying to image. The interference pattern formed by the reference wave and the object wave is what is recorded on the holographic film. So if the reference wave is described by  $\mathbf{E}_{ref}$  and the object wave by  $\mathbf{E}_{obj}$ , the intensity recorded on the film is

$$I = |\mathbf{E}_{ref} + \mathbf{E}_{obj}|^2 = E_{ref}^2 + E_{obj}^2 + 2\text{Re} [\mathbf{E}_{ref} \cdot \mathbf{E}^*_{obj}] .$$

The first two terms on the right hand side of this equation correspond to the separate intensities of the reference and object waves. The final term on the right hand side is what contains information about the relative phase of the two beams. The way we retrieve this information is illustrated in the right half of Figure 2.1. When the developed holographic film is illuminated with the reference wave, an exact copy of the object wave is output on the other side of the hologram at the angle (relative to the reference wave) at which it was input [7]. There is also a beam output at the opposite angle which is the complex conjugate of the object beam, and a transmitted

beam which has the same form as the reference.

What we want to do in the context of this experiment is image a mode of laser light rather than an object. Since we don't have the mode we are interested in to begin with, it is easiest to generate the necessary holograms using a computer. For reference, here is the spatial amplitude distribution of an LG mode with index  $l$  (note that it matches the form of Equation 2.4):

$$u_l(r, \phi, z) = \frac{C_l^{LG}}{w(z)} \left( \frac{r\sqrt{2}}{w(z)} \right)^{|l|} \exp \left( -\frac{r^2}{w^2(z)} \right) L_0^{|l|} \left( \frac{2r^2}{w^2(z)} \right) \times \exp \left( \frac{r^2}{2(z^2 + z_R^2)} \right) \exp(il\phi) \exp \left( i(|l| + 1)\arctan \left( \frac{z}{z_R} \right) \right) \exp(ikz). \quad (2.7)$$

Here,  $C_l^{LG}$  is a normalization constant,  $w(z)$  is the beam waist given by

$$w(z) = w(0) \sqrt{1 + \frac{z^2}{z_R^2}}$$

$z_R = \pi w(0)^2 / \lambda$  is the Rayleigh range, and  $L_0^{|l|}(2r^2/w^2(z))$  is a generalized Laguerre polynomial given by [3], [8]

$$L_0^{|l|}(x) = \frac{e^x}{x^{|l|}} \frac{d}{dx} (e^{-x} x^{|l|}).$$

If we simulate the interference of an  $l = 1$  LG beam coming in at an angle (like the object wave in Figure 2.1) with a Gaussian reference beam using *Mathematica*, we see the intensity pattern in Figure 2.2. This looks much like the forked diffraction grating in Figure 1.3 enclosed within a Gaussian intensity envelope.

As it turns out, this analysis is slightly overcomplicated for our purposes. The important difference between a Gaussian beam and Laguerre-Gaussian beam is the phase  $e^{il\phi}$ . At the most fundamental level, all we want to do is impart a phase  $e^{il\phi}$  onto a beam that has a tilt in, say, the  $x$ -direction. In other words, the object beam has a phase  $e^{il\phi}$  relative to the reference beam, and the reference beam has a phase  $e^{ikx}$  relative to the object beam [9]. The intensity profile of this simplified hologram is then

$$I(x, y) = |e^{ikx} + e^{il\phi}|^2 = 2 + 2\cos(kx - l\phi) = 2 + 2\cos(kx - l\arctan(y/x)). \quad (2.8)$$

In this equation,  $|l|$  varies the number of forks in the pattern, the sign of  $l$  varies whether the pattern is oriented upright or inverted, and  $k$  varies the spacing of the fringes. A few holograms created with this intensity profile are shown in Figure 2.3. Since  $(e^{il\phi})^* = e^{-il\phi} = e^{i(-l)\phi}$ , these holograms generate an LG mode with index  $l$  in the first diffracted order and an LG mode with index  $-l$  in the first order on the opposite side of the central transmitted beam.

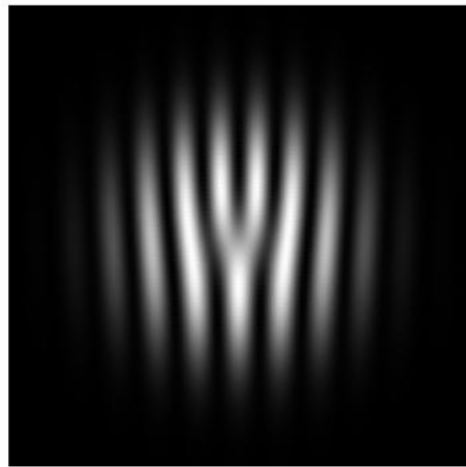


Figure 2.2: Simulated interference of tilted LG beam and Gaussian reference beam.

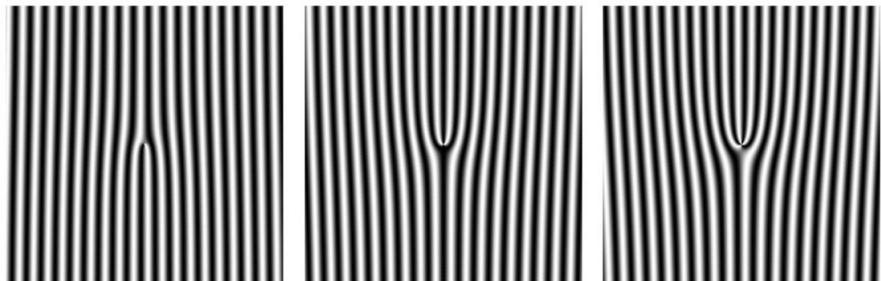


Figure 2.3: Starting on the left and going right,  $l = -1, +2$ , and  $+3$  holograms.

## 2.3 Interference of the LG Modes

In order to predict what the interference (or superposition) of two LG modes would look like we could plug Equation 2.7 into *Mathematica* and plot the results (in fact

we will do just that in Section 3.3). But Equation 2.7 is unnecessarily cumbersome if all we want to do is gain a qualitative understanding of what is going on when two LG modes interfere. Since Equation 2.7 matches the form of Equation 2.4, we can simplify things by ignoring the dependence of  $u_l(r, \phi, z)$  on  $r$  and  $z$  and just looking at the interference of the phase factors  $e^{il\phi}$ .

In this simplified model, the intensity pattern of a superposition of beams with  $l$ -values  $l_1$  and  $l_2$  is

$$I(\phi) = |e^{il_1\phi} + e^{il_2\phi} e^{i\delta}|^2 = 2 + 2\cos((l_1 - l_2)\phi - \delta). \quad (2.9)$$

Here,  $\delta$  represents some relative phase between the two beams. Since the intensity has a sinusoidal dependence on  $\phi$ , we can first think about how many times  $I(\phi)$  goes to zero through one full cycle of  $\phi$ . Note that  $I(\phi)$  is zero when  $\cos((l_1 - l_2)\phi - \delta)$  is  $-1$ . This occurs when

$$(l_1 - l_2)\phi_{dark} - \delta = (2n + 1)\pi \implies \phi_{dark} = \frac{(2n + 1)\pi + \delta}{(l_1 - l_2)} \quad (2.10)$$

where  $n$  is an integer. In the case where  $(l_1 - l_2) = 1$ , there is one value of  $\phi_{dark}$  between 0 and  $2\pi$  for fixed  $\delta$ . In fact, the number of dark regions is exactly the difference between  $l_1$  and  $l_2$ . Figure 2.4 shows example intensity patterns for three different values of  $(l_1 - l_2)$ . In the special case where  $l_1 = l_2$ , the intensity is constant in  $\phi$  and varies up and down with the phase difference  $\delta$ .

From Equation 2.9, we can also see that changing the relative phase  $\delta$  between the two beams has the effect of rotating the intensity pattern in the plane. This feature is demonstrated in Figure 2.5. We'll see in Section 3.3 that the principles discovered here (that the difference in the index  $l$  determines the number of dark regions and that changing  $\delta$  rotates the intensity pattern) apply both in theory and practice when we work with the LG modes in their full form.

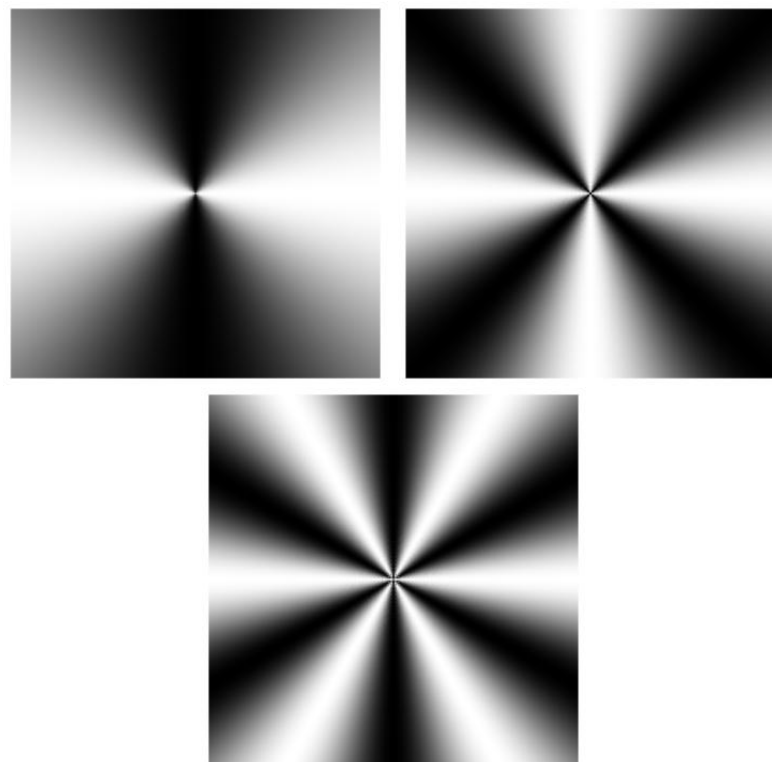


Figure 2.4: Starting top-left and going clockwise, interference patterns for  $l_1 - l_2 = 2, 4$ , and  $6$  ( $\delta = 0$ ).

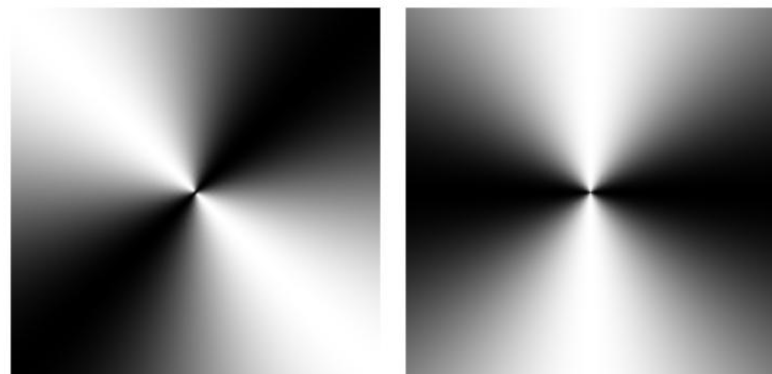


Figure 2.5: Intensity patterns for  $l_1 - l_2 = 2$  with  $\delta = \pi/2$  and  $\delta = \pi$ .

# Chapter 3

## Experiment

### 3.1 Table Setup for Generating and Interfering LG Modes

As mentioned in Chapter 1, we used a Spacial Light Modulator (SLM) to display the computer-generated holograms needed to transform a simple Gaussian beam into a Laguerre-Gaussian beam. The SLM has a liquid crystal display (LCD) on it that is set in front of a mirror. Each pixel on the LCD contains a birefringent liquid crystal. If a voltage is applied to the pixel, the liquid crystal modifies the index of refraction for one polarization direction by an amount proportional to the voltage. If the laser polarization is parallel to the the axis of the crystals, this creates a phase grating which allows the LCD to mimic whatever is on the computer monitor it is connected to in exactly the same way as a common LCD projector. Generating the LG modes does not necessarily require any more complicated experimental setup than a laser incident on the SLM. Superposing two LG modes, however, does require a little more ingenuity. In general, we would like to be able to superpose any two LG modes, but we only have one SLM available in the lab. The table setup which solves this problem is shown in Figure 3.1.

The interferometer in Figure 3.1 is a modified version of a common-path Sagnac

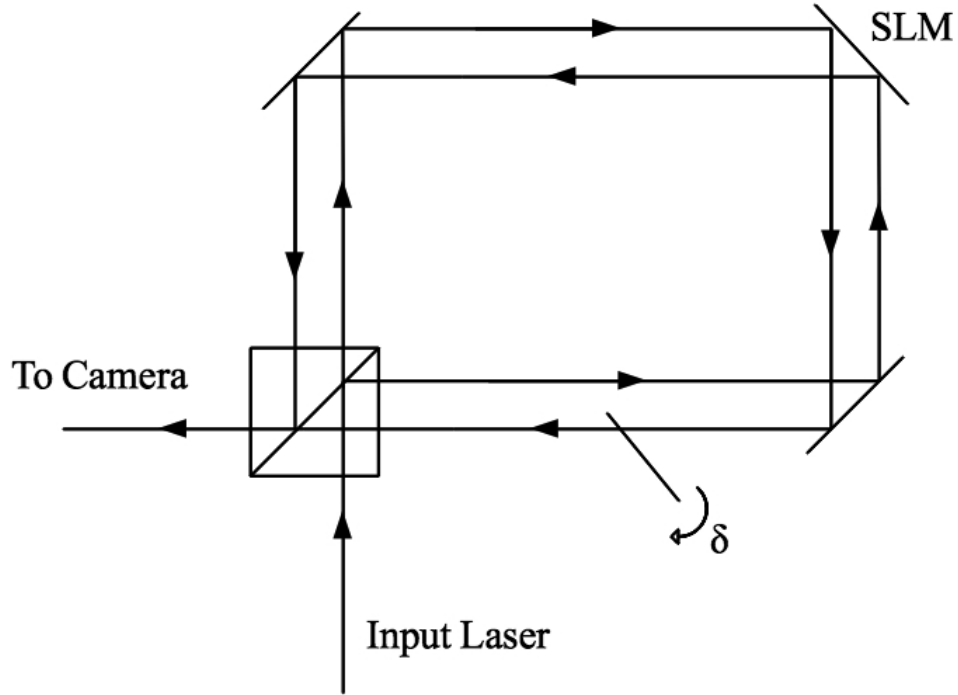


Figure 3.1: Modified Sagnac interferometer used to form superpositions of LG modes.

interferometer. The two beams in this interferometer travel essentially the same path (in opposite directions), but there is some lateral separation between the two beams. This means that the two beams both hit the SLM, but in different places. So, we can generate two different LG modes with one SLM by placing different holograms at the two positions where the two beams hit the SLM, aligning everything so that it is the first order diffracted beams which recombine at the beam splitter. The component towards the bottom of Figure 3.1 is a glass slide inserted at an angle into one of the beams. By varying the angle of the slide, we can vary the relative phase  $\delta$  between the two beams.

It's also worth noting that before the laser was input to the interferometer, it went through a linear polarizer, a half-wave plate, a neutral density filter, and it was coupled to a single mode optical fiber. The linear polarizer allowed us to vary the intensity of the beam while the half-wave plate rotated the polarization of the beam to achieve maximum diffraction efficiency. The neutral density filter simply cut down

the intensity of the laser so that the camera wouldn't be saturated. Finally, the optical fiber ensured that the beam was in a pure Gaussian mode. A complete diagram of the table setup, including the additional interferometer described in Section 3.4, is given in Appendix A.

The camera we used in the lab was a *Basler acA 1600* USB 3.0 digital camera. This camera has a resolution of  $1628 \times 1236$  and a pixel size of  $4.4\mu\text{m} \times 4.4\mu\text{m}$ . In order to manage both the holograms on the SLM and the images from the USB camera at the same time, it was helpful to use two computer monitors. One monitor was solely for controlling the SLM. We ended up writing a program in *LabVIEW* which could open two holograms at specified positions on the SLM monitor, move the holograms around on the monitor, change the size of the holograms, and switch holograms for generating different LG modes. This program is discussed briefly in Appendix B. With this setup, we could have total control over the holograms displayed on the SLM while taking pictures with the camera using the second monitor.

## 3.2 Generating Single LG Modes

The very first question we can ask once our table is completely set-up is whether we can generate single LG modes with some degree of purity. In other words, we want to make sure that the holograms described in Section 2.2 work as we expect them to. In generating these single modes, we used the same experimental setup detailed in Figure 3.1. Instead of displaying two holograms on the SLM, however, we just displayed one so that we would have only one first-order diffracted beam incident on the camera. Experimental results are compared with theoretical predictions for an  $l = 1$  LG mode in Figure 3.2.

In Figure 3.2, we can qualitatively see that the theory and experiment are very similar. It's likely that what we have generated is indeed an  $l = 1$  LG mode. To get a more quantitative measure of the agreement between theory and experiment, we

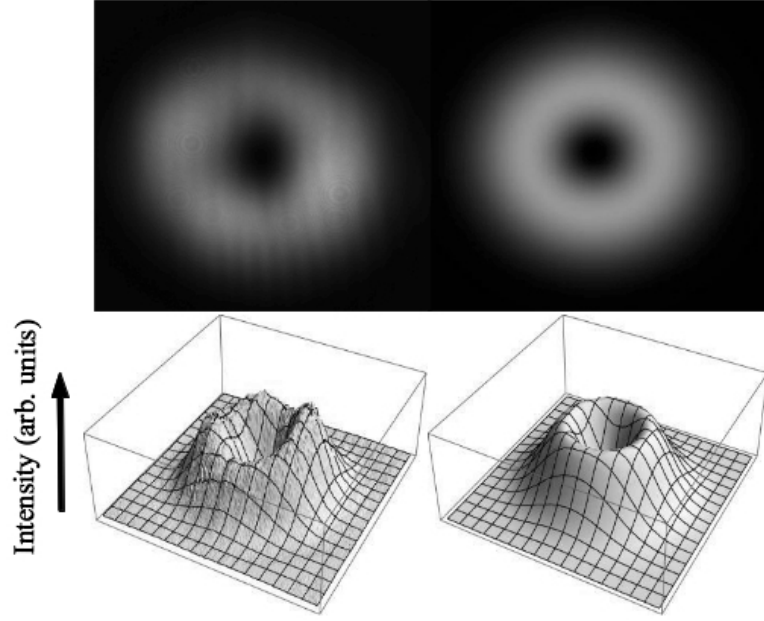


Figure 3.2: In the top-left, a photograph of the first diffracted beam using an  $l = 1$  hologram. This photograph is  $300 \times 300$  pixels with an exposure time of 10ms. In the bottom left, the intensity of each pixel from the image above plotted vertically. The top-right and bottom-right images are theoretical fits of the data on the left to Equation 3.1.

first fit the data to a theoretical model found by taking the magnitude squared of the amplitude distribution in Equation 2.7 (for simplicity, we evaluate at  $z = 0$  and use  $w_0 \equiv w(0)$ ):

$$|u_l(r, \phi, 0)|^2 = \frac{I_0}{w_0^2} \left( \frac{r\sqrt{2}}{w_0} \right)^{2|l|} \exp \left( -\frac{2r^2}{w_0^2} \right) \exp \left( \frac{r^2}{z_R^2} \right) \left[ L_0^{|l|} \left( \frac{2r^2}{w_0^2} \right) \right]^2 \quad (3.1)$$

If we recall that  $r = \sqrt{x^2 + y^2}$ , then the only fitting parameters in Equation 3.1 are the overall amplitude  $I_0$ , the beam waist  $w_0$ , and the  $(x, y)$  position of the center of the beam. Using *Mathematica*'s `NonLinearModelFit` function, we found the theoretical intensity pattern plotted in the bottom-right of Figure 3.2. To then quantify the agreement between the data and the fit, we normalize the intensities  $I_{fit}(x, y)$  and

$I_{data}(x, y)$  such that

$$\iint_A I_{fit}(x, y) dx dy = \iint_A I_{data}(x, y) dx dy = 1 \quad (3.2)$$

where A is the region captured in the photograph. Since intensities are always non-negative, it follows that

$$0 \leq \iint_A \sqrt{I_{fit} I_{data}} dx dy \leq 1. \quad (3.3)$$

Because of the condition in Equation 3.2, if the integral in Equation 3.3 exactly equals 1, then  $I_{fit} = I_{data}$  everywhere in the region. The closer this integral is to 1, the more completely  $I_{fit}$  and  $I_{data}$  overlap.

Using *Mathematica* again to numerically evaluate the integrals in Equations 3.2 and 3.3, we found that the overlap between  $I_{fit}$  and  $I_{data}$  was about 0.980 while the fitted value of  $w_0$  was  $340\mu\text{m}$  for the  $l = 1$  mode pictured in Figure 3.2. So, we can say with confidence that we can generate an  $l = 1$  LG mode using the SLM in the expected manner. The parameter  $w_0$ , however, is only the true waist size for a simple Gaussian ( $l = 0$ ) beam. To get a better measure of the width of the beam, we can maximize Equation 3.1 with respect to  $r$  using *Mathematica* to set the derivative of Equation 3.1 equal to zero and solve for  $r$ . If we call the value of  $r$  which gives the maximum intensity  $r_{waist}$ , then

$$r_{waist} = w_0 z_R \sqrt{\frac{|l|}{z_R^2 - w_0^2}} \quad (3.4)$$

where, again,  $z_R = \pi w_0^2 / \lambda$  (we used a laser with  $\lambda = 532\text{nm}$ ). Note that this equation only represents the beam waist for non-zero values of  $l$ . With this definition,  $r_{waist}$  for the fit in Figure 3.2 was  $240\mu\text{m}$ . Similar data using an  $l = 2$  hologram is shown in Figure 3.3. The calculated overlap between  $I_{fit}$  and  $I_{data}$  for this mode was 0.910 while the  $r_{waist}$  for the fit was  $323\mu\text{m}$ .

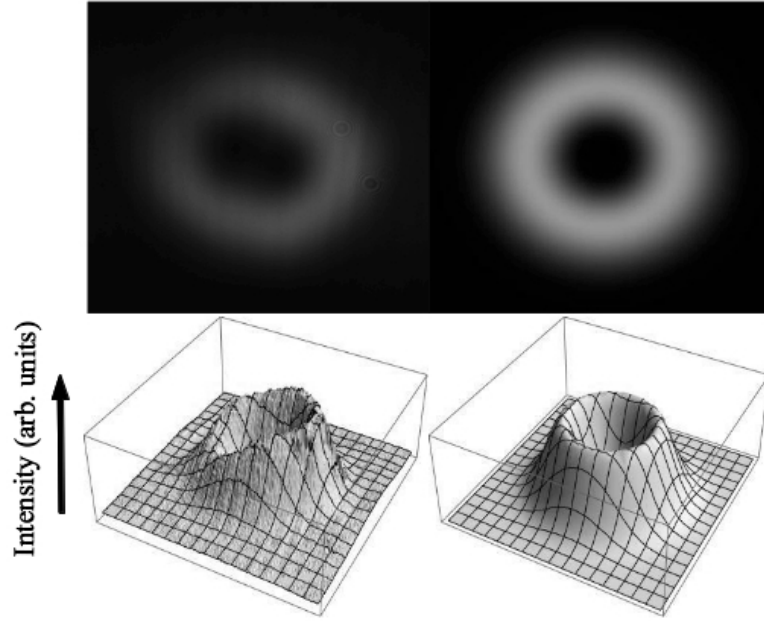


Figure 3.3: In the top-left, a photograph of the first diffracted beam using an  $l = 2$  hologram. This photograph is  $360 \times 360$  pixels with an exposure time of 10ms. In the bottom left, the intensity of each pixel from the image above plotted vertically. The top-right and bottom-right images are theoretical fits of the data on the left to Equation 3.1.

Although the overlap is strong between the data and the fitted curve for  $l = 2$ , the photograph in the top-left of Figure 3.3 shows some asymmetry in the central dark region. The reason for this is not entirely clear. We found that changing the alignment of the hologram on the SLM did not clear up this problem. It may be that there were irregularities in the input laser beam (i.e. the input beam may not have been in a pure Gaussian mode) which were exacerbated as we increased the value of  $l$  in the hologram displayed on the SLM. In Figure 3.4, we can see that the asymmetry is indeed worse for higher  $l$ . In the case of an  $l = 3$  hologram, the overlap between the data and the fitted curve was 0.894 while  $r_{waist}$  for the fit was  $426\mu\text{m}$ .

It's interesting to note that in Figures 3.2 through 3.4, the first diffracted beams appear to be getting dimmer as the order of the hologram increases. The simplest

explanation for this trend is illuminated by Figure 3.5, where photographs of the first diffracted beams are shown on the same scale for  $l = 1$ ,  $l = 2$ , and  $l = 3$  holograms. In Figure 3.5, it's clear that as  $l$  increases, the waist size of the output beam increases. Assuming that the same amount of power is channeled into the first diffracted beam for each  $l$ , this means that the same amount of power is being spread over larger areas for larger  $l$ . Hence, the output beam seems dimmer for larger  $l$ . It is also possible that the power in the first diffracted beam is not the same for each  $l$ , but this would most likely be an effect secondary to the effect of increasing waist size.

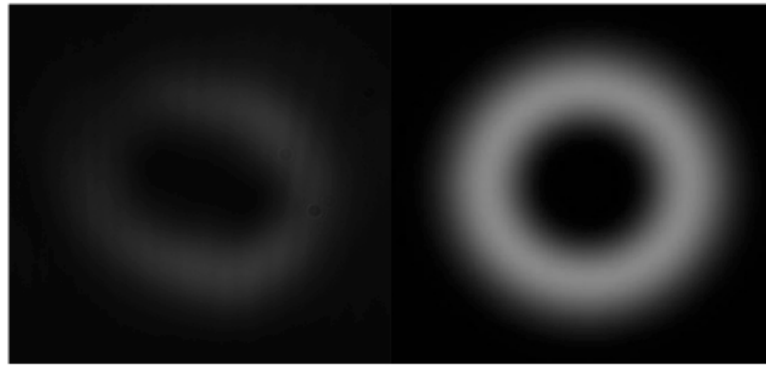


Figure 3.4: On the left, a photograph of the first diffracted beam using an  $l = 3$  hologram. This photograph is  $400 \times 400$  pixels with an exposure time of 10ms. On the right, a theoretical fit of the data to Equation 3.1.

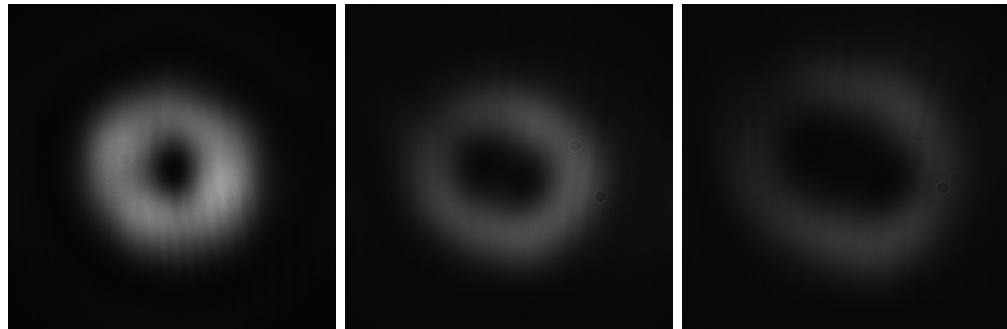


Figure 3.5: Starting on the left and going right, first-order diffracted beams for  $l = 1$ ,  $l = 2$ , and  $l = 3$  holograms shown on the same scale (each photograph had an exposure time of 10ms and was cropped to  $360 \times 360$  pixels).

### 3.3 Superpositions of LG Modes

To create superpositions of LG modes, we used the experimental setup of Figure 3.1, placing two holograms on the SLM instead of one. In order to align the interferometer, we found it easiest to first place simple diffraction gratings on the SLM so that we had Gaussian beams in the first diffracted order. This way, we would know the two output beams were perfectly aligned when the intensity of the spot on the camera faded in and out as we changed the relative phase (as opposed to having fringes going across the spot in some direction). With the interferometer aligned, we then switched the holograms on the SLM to, say,  $l = 1$  and  $l = -1$ , and achieved the results laid out in Figure 3.6.

In the top row of Figure 3.6, we see simulated interference patterns for the addition of positive and negative LG modes. These were generated in *Mathematica* using Equation 2.7 in its full form. Note the similarities of these patterns to the ones illustrated in Figure 2.4. In each case, the difference between the values of  $l$  in the two beams is equal to the number of bright spots (or dark spots). The simulated patterns are to be compared with the photographs in the second row of Figure 3.6. Although there are a few minor asymmetries, especially for the higher order patterns, the shape of each simulated pattern closely matches the patterns in the photographs. For example, the overlap between the data and a fitted curve for the addition of  $l = 1$  and  $l = -1$  modes was 0.955.

The other feature being illustrated in Figure 3.6 is the way that the interference patterns change as the relative phase between the two beams is varied. Going down any one of the columns in Figure 3.6 corresponds to making small changes in the phase of one of the beams (by tilting the glass slide of Figure 3.1). As we expected based on the predictions of Figure 2.5, the patterns rotate about their centers as the phase is adjusted. This is true even for the superpositions of higher order modes. The shape of the interference pattern, for the most part, remains unchanged as the entire pattern rotates. We also note that, as with single LG modes, the brightness of

the interference patterns diminishes as we increase the magnitude of the  $l$  values in the component beams because of the extra area which the higher-order patterns take up.

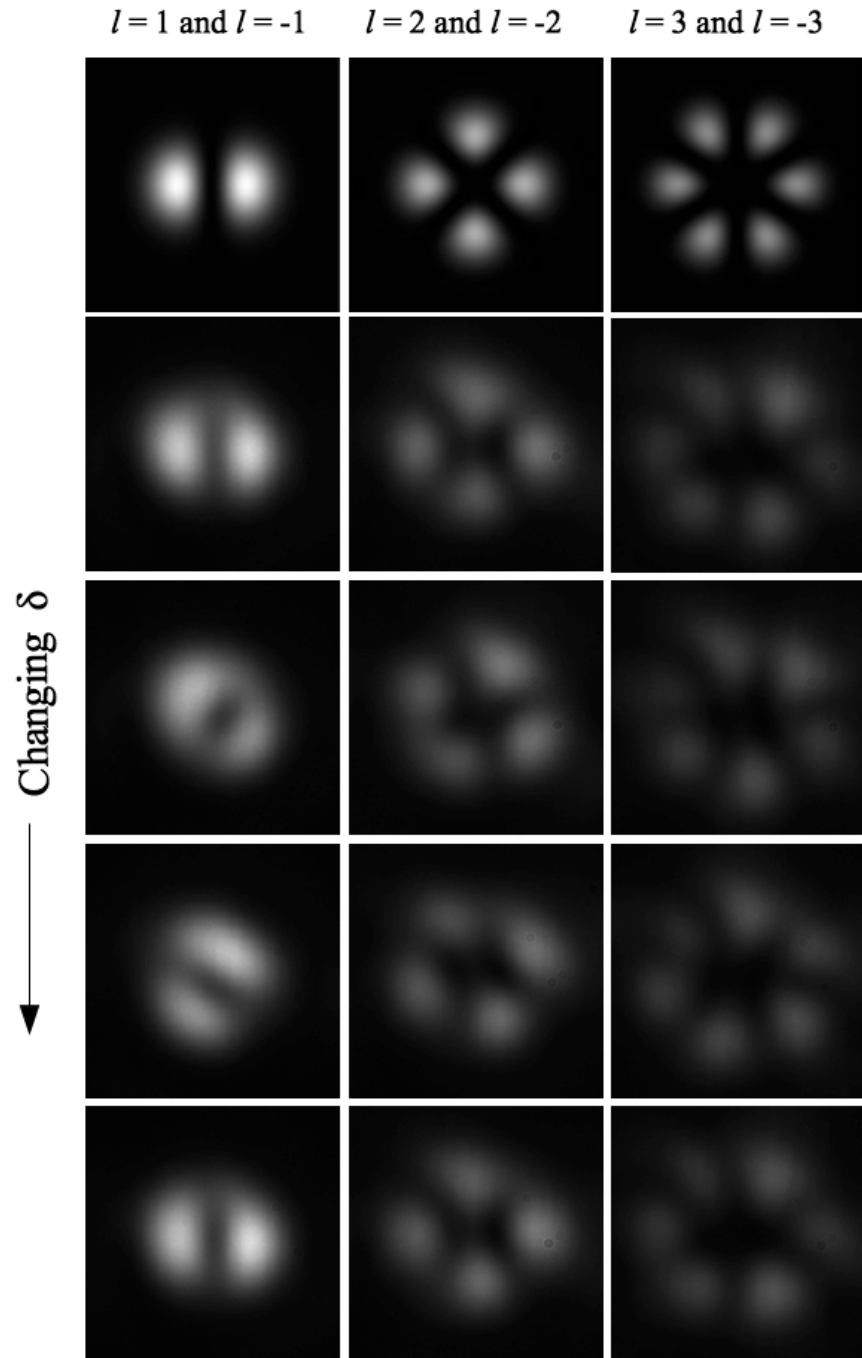


Figure 3.6: In the top row, theoretical intensity patterns for the superpositions of LG modes labeled above. Subsequent rows show photographs of superpositions with each row having slightly more relative phase between the interfering beams than the row above. Here, each photograph had an exposure time of 10ms and was cropped to  $320 \times 320$  pixels.

### 3.4 Sorting Even and Odd LG Modes

Beyond generating and interfering LG modes, we'd also like to be able to extract information about the orbital angular momentum of a laser beam. This can be done using the holograms of Section 2.2. If, for example, an  $l = 1$  LG mode is incident on an  $l = -1$  hologram, the first diffracted beam will be in a simple Gaussian mode which can be coupled to a single mode fiber. Modes besides  $l = 1$  will not produce a Gaussian in the first diffracted beam. This method is simple, but it can only test for single LG modes. It cannot tell us exactly what the orbital angular momentum of a laser beam is. We explored a more general interferometric method of measuring orbital angular momentum laid out in Ref. [10].

The interferometric method of sorting relies on an optical device called a Dove prism. The workings of the Dove prism are illustrated in Figure 3.7. Light incident on the angled sides of a Dove prism is refracted and then goes through a total internal reflection off of the lower base of the prism. That total internal reflection flips the transverse profile of the beam over the axis which runs along the lower base.

The design of the interferometer we used for sorting odd and even modes is shown in Figure 3.8. This interferometer is essentially the interferometer in Figure 3.1 with Dove prisms in each arm. The reason for having two Dove prisms oriented at a  $90^\circ$  angle to each other is illustrated in Figure 3.9. In Figure 3.9, we see phase profiles for an odd ( $l = 1$ ) and an even ( $l = 2$ ) LG mode. These phase profiles are something like what you would see looking down the beam axis if your eyes could detect electric fields.

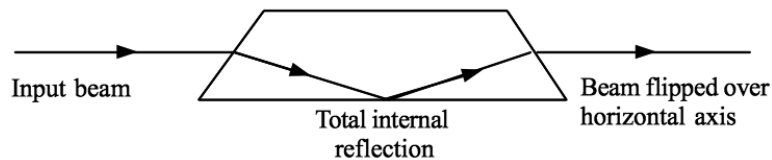


Figure 3.7: An illustration of the way a Dove prism flips a laser beam over the axis defined by its lower base.

Looking closely at the phase profiles, we see that if we flip an odd mode horizontally in one arm of the interferometer and vertically in the other, the products are  $\pi$  out of phase with each other. If we do the same thing to an even mode, however, the products are in phase with each other. Thus, even modes will interfere constructively at one output of the interferometer and odd modes will interfere constructively at the other. In other words, depending on  $\delta$ , only even modes will exit through one port and only odd modes will exit through the other. This is the reason for placing an extra mirror at the second output of the interferometer and redirecting the output to the camera.

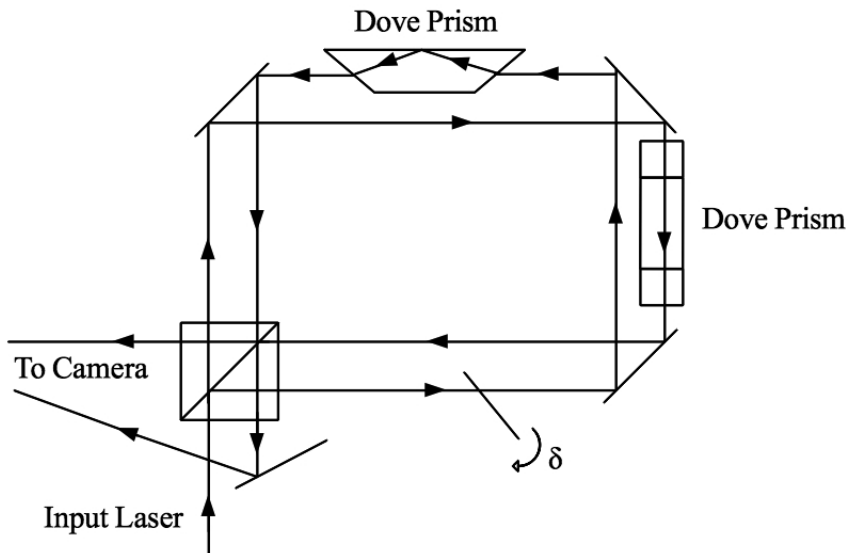


Figure 3.8: Altered version of the interferometer in Figure 3.1 with Dove prisms in each arm. The Dove prisms are oriented at  $90^\circ$  with respect to each other for sorting odd and even LG modes.

Our table was set up so that the output of the interferometer creating superpositions of LG modes was the input for the sorting interferometer (see Appendix A). The simplest superposition we could sort was a superposition of an  $l = 1$  state with an  $l = 0$  state. Visually, sorting this state would also be easier since the  $l = 0$  state is a simple Gaussian which has no central dark spot. Some photographs of the two sorted output beams side-by-side are shown in Figure 3.10. In the first photograph

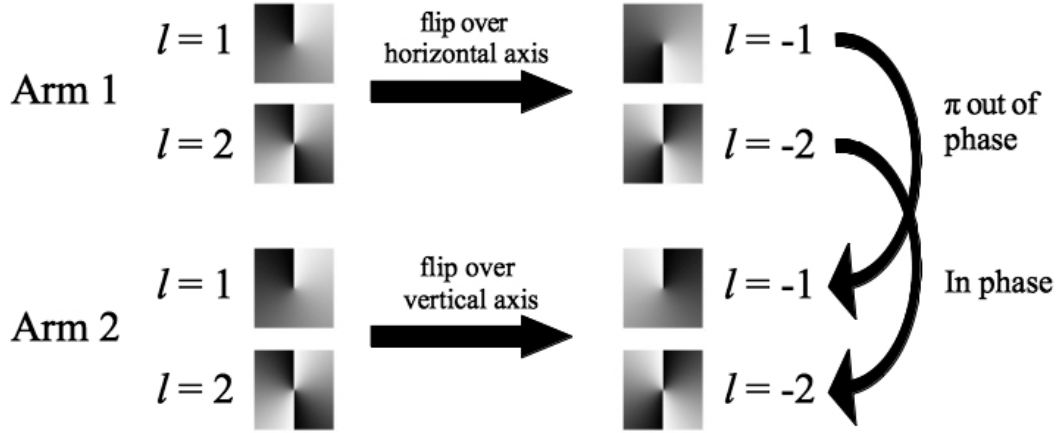


Figure 3.9: Illustration of what happens to even and odd modes in the two arms of our sorting interferometer.

of Figure 3.10 we can clearly see an  $l = 0$  mode on the left and an  $l = 1$  mode on the right. Subsequent photographs in Figure 3.10 show how the two outputs change as the relative phase between the two arms of the interferometer is adjusted. The output beam on the right begins in an  $l = 1$  state, morphs into an  $l = 0$  state, and then morphs back into an  $l = 1$  state (while the left side does the opposite). This is exactly how we should expect the sorting interferometer to work.

Although this method of sorting LG modes is not perfectly general, it is possible to sort the even and odd modes further by putting each through additional interferometers with Dove prisms [10]. The idea is to cut the angle between the Dove prism orientations in half with each additional interferometer and so split the superpositions into two further categories. For example, if you have a beam of even modes from the first interferometer and put that through an interferometer where the Dove prisms are oriented at  $45^\circ$  with respect to each other, you can sort the even modes into modes in which  $l$  is an even multiple of two and modes in which  $l$  is an odd multiple of two. So, in an application where you might know exactly how many modes you will have to sort, you can build the number of interferometers required and have a perfectly general sorting mechanism.

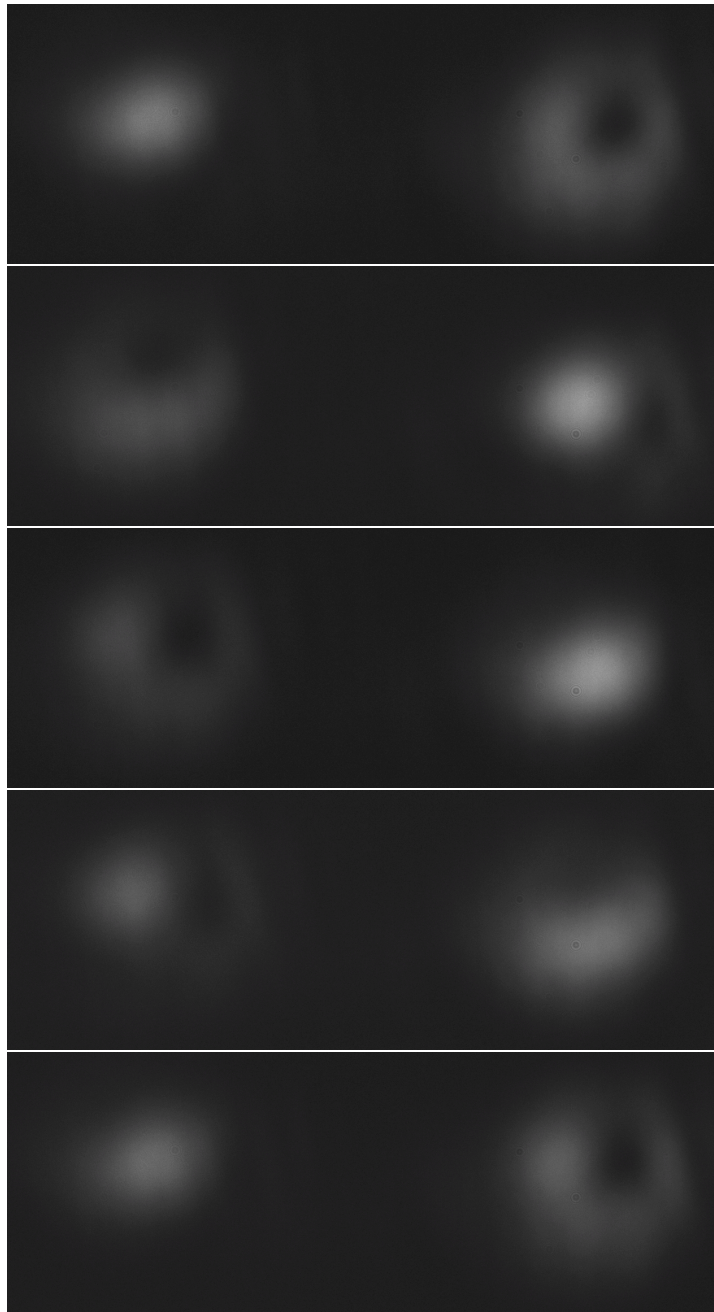


Figure 3.10: Photographs of the two outputs of the sorting interferometer when the input is a superposition of  $l = 0$  and  $l = 1$  states. Each photograph has a slight increase in the relative phase  $\delta$  from the one above it. If the top photograph has  $\delta = 0$ , then the third photograph has  $\delta = \pi$ , and the final photograph has  $\delta = 2\pi$ . The photographs all have resolution  $1260 \times 460$  pixels and were taken with an exposure time of 50 ms.

# Chapter 4

## Conclusion

Here we have demonstrated experimental methods for generating Laguerre-Gaussian modes from a simple Gaussian mode, interfering LG modes and predicting the form of the interference pattern, and finally, sorting odd and even LG modes. We've found that although the first diffracted beams from higher order holograms contain some unexpected asymmetries, the overlap between the experimental intensity patterns and the fitted theoretical curves is high for  $l = 1, 2$ , and  $3$ . In fact, we've shown that we can generate all of the LG modes with indices  $l = -3$  through  $l = 3$  (the negative LG modes have identical intensity patterns to those shown in Figures 3.2-3.4).

Using these single LG modes, we've been able to form interference patterns between positive and negative modes and not only predict the shape of the intensity patterns, but also the fact that the patterns rotate as the relative phase of the two interfering beams is altered. The rotation of the interference patterns is evidence of the twisting phase fronts of the LG modes, which cannot be observed from the intensity patterns of single modes alone. In sorting an  $l = 0$  mode from an  $l = 1$  mode, we've also seen how varying the relative phase between the two modes can switch the outputs at which odd and even modes constructively interfere.

There are two strengths of the experimental methods described here which are worth noting. First, all of the methods are simple enough to be performed in an

undergraduate laboratory. The most advanced piece of equipment necessary was the Spacial Light Modulator. Second, all of the methods can, in principle, work using single photon sources ([4],[10]). This means that the methods could be useful in performing quantum mechanical experiments. In this work, we haven't thought much about the LG modes in a quantum mechanical context, yet it is their quantum properties which motivate much of the current research being done with LG modes. The LG modes correspond to a basis of orbital angular momentum states which is infinite in dimension, discrete, orthogonal, and complete. It is hoped that the methods set out here will enable future undergraduate researchers to explore quantum phenomena in this unique basis.

## Appendix A

### Detailed Experimental Setup

Here we present a more complete picture of the experimental setup used in this research. Figure A.1 is a photograph of the lab table as it was set up for sorting odd and even LG modes. Figure A.2 is a detailed diagram of the same setup.

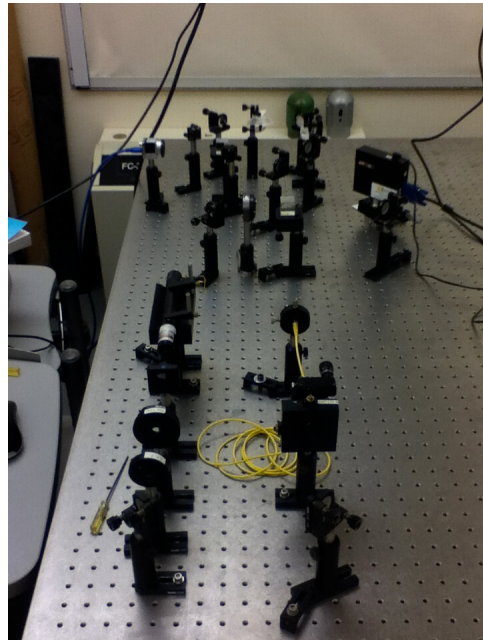


Figure A.1: Photograph of our table setup including both the generating interferometer and the sorting interferometer.

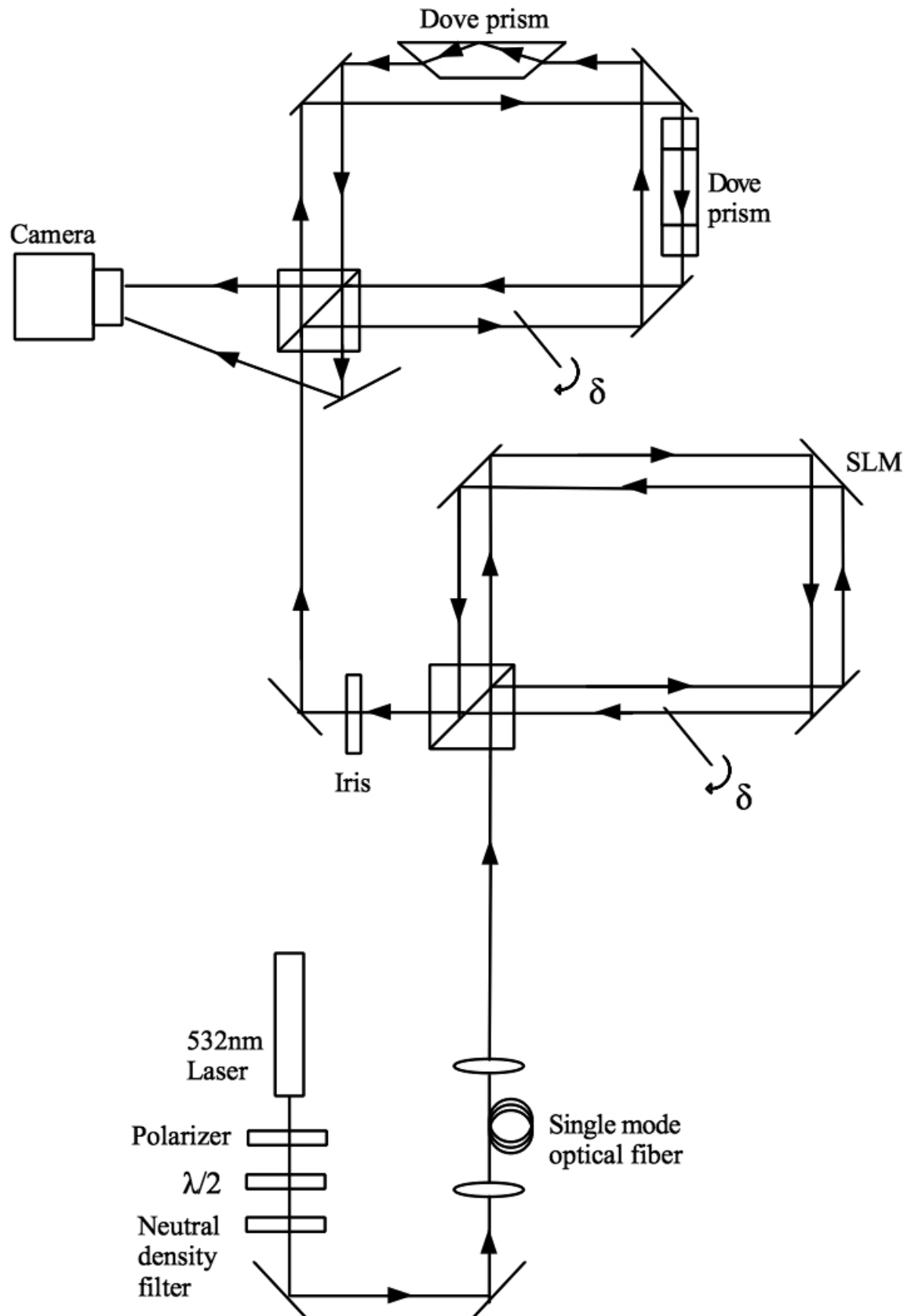


Figure A.2: Detailed diagram of the table setup shown in Figure A.1.

# Appendix B

## *LabVIEW* Programming

After generating the holograms of Section 2.2 in *Mathematica*, we wanted to be able to display holograms on the monitor being mirrored by the SLM. We also wanted to be able to move the holograms around on the screen, zoom in and out, and change each hologram to different orders. Since *LabVIEW* provides pre-built programs made for opening external windows and performing operations on them, it was a natural choice for solving these problems. Figure B.1 shows the block diagram of a program called WindSettings.vi written to take the identifying number of a previously-opened window and set its center point, zoom factor, width, height, and screen coordinates. There is also an option to bring the window to the front.

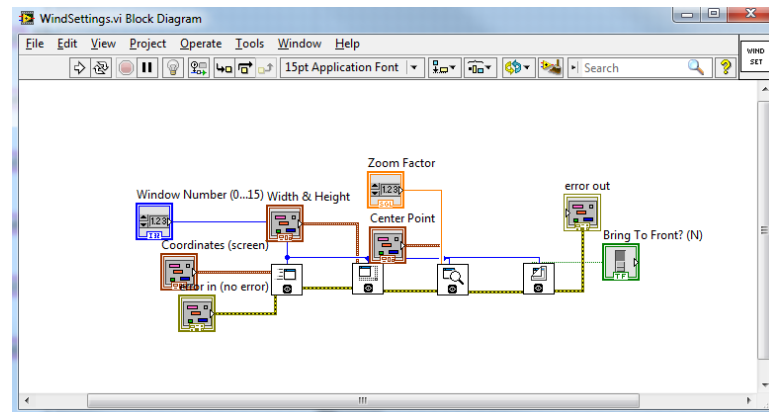


Figure B.1: Block diagram for WindSettings.vi which sets parameters for one window.

The front panel of the main program which makes use of WindSettings.vi is shown in Figure B.2. This program, called Open External Window.vi, opens several windows and puts a single hologram in each. The windows are split into two groups (right and left), within which the zoom, center, and position coordinates are all the same. This means that only two holograms are visible on the monitor at a time because one hologram will always be in front. To change which hologram is in front, the user can click the buttons labeled with the order of the hologram. A portion of the block diagram for this program is shown in Figure B.3. There we see how the program opens several windows from image files and then sets their parameters using WindSettings.vi.

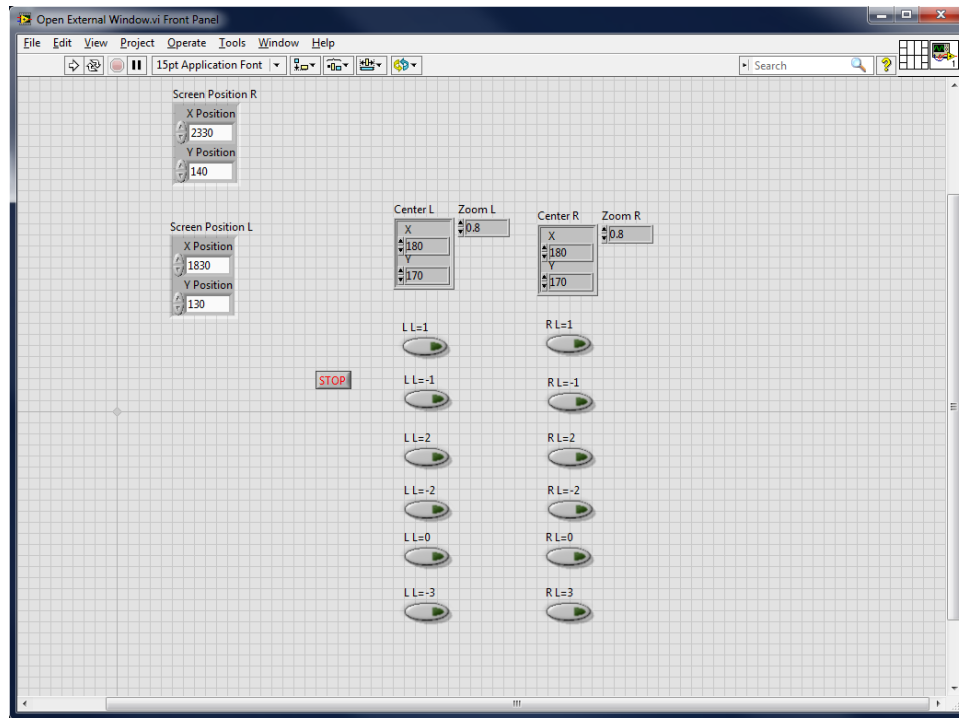


Figure B.2: Front panel for Open External Window.vi.

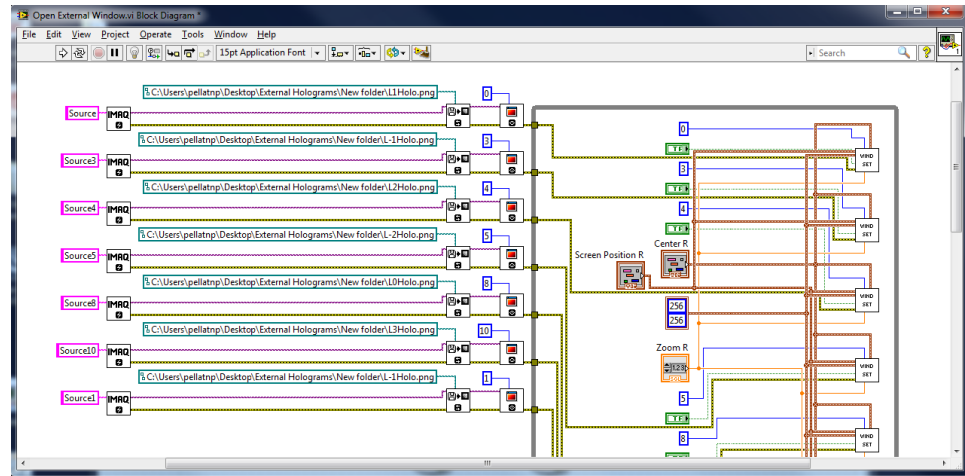


Figure B.3: Block diagram for Open External Window.vi.

Finally, in Figure B.4 we include a screen shot of the program used to take photographs with our camera. This program was provided by Basler, the makers of the camera. Along the top panel are some controls for taking single shots, taking a continuous shot, and saving the captured image. There are many different settings available on the left. The setting most often adjusted in this research was the exposure time.

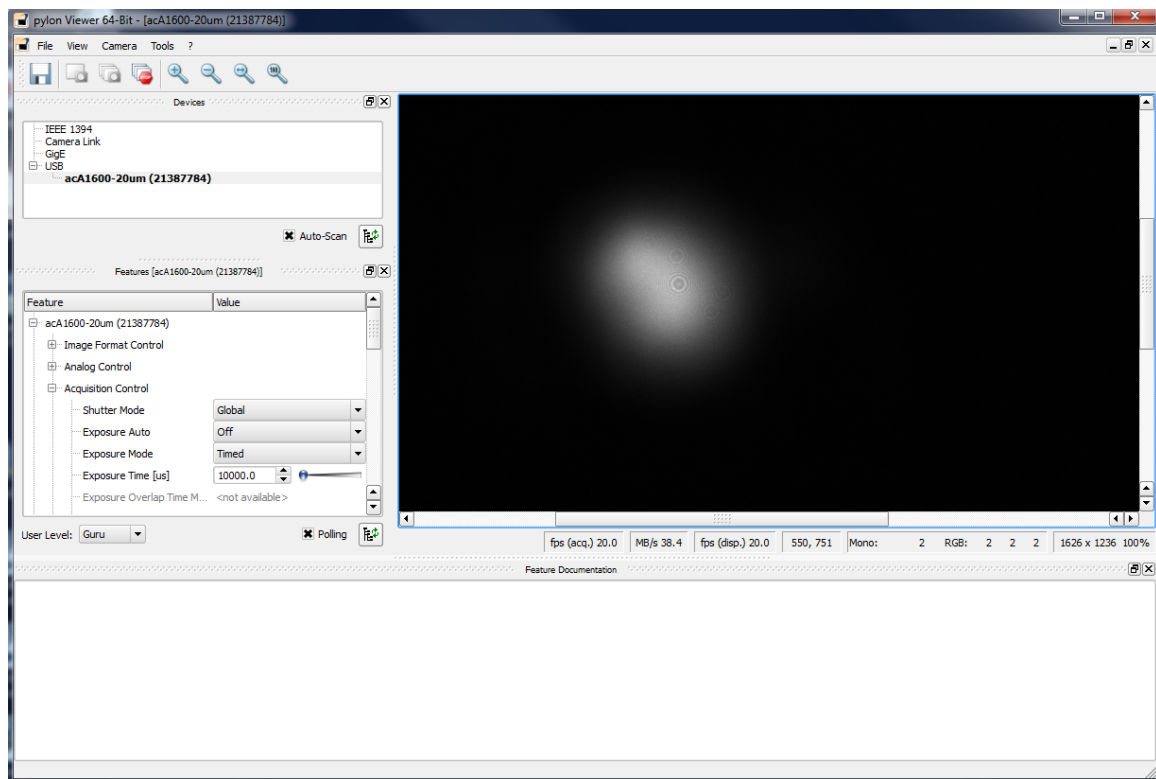


Figure B.4: Basler program used to capture photographs with the USB camera used in the lab.

# Bibliography

- [1] Miles Padgett, Johannes Courtial, and Les Allen. “Light’s orbital angular momentum.” *Physics Today* 57.5 (2004): 35-40.
- [2] Derek Huang, Henry Timmers, Adam Roberts, Niranjan Shivaram, Arvinder S. Sandhu. “A low-cost spatial light modulator for use in undergraduate and graduate optics labs.” *Am. J. Phys.* 80, 211 (2012).
- [3] L. Allen, M. J. Padgett, and M. Babiker. “IV The orbital angular momentum of light.” *Progress in Optics* 39 (1999): 291-372.
- [4] Mair, Alois, et al. “Entanglement of the orbital angular momentum states of photons.” *Nature* 412.6844 (2001): 313-316.
- [5] Franke-Arnold, Sonja, et al. “Uncertainty principle for angular position and angular momentum.” *New Journal of Physics* 6.1 (2004): 103.
- [6] Griffiths, David J. *Introduction to Electrodynamics*. 3rd ed. Upper Saddle River, New Jersey: Prentice Hall, 1999. Print.
- [7] Kenyon, Ian R. *The Light Fantastic* 2nd ed. New York: Oxford University Press, 2011. Print.
- [8] Abramowitz, Milton and Stegun, Irene A. “Orthogonal Polynomials” *Handbook of Mathematical Functions*. Washington, D.C.: National Bureau of Standards, 1964. Print.

- [9] Carpentier, Michinel, Salgueiro, and Olivieri. “Making optical vortices with computer-generated holograms.” *Am. J. Phys.* 76, 916 (2008): 916-921.
- [10] Leach, Padgett, Barnett, Franke-Arnold, and Courtial. “Measuring the Orbital Angular Momentum of a Single Photon.” *Phys. Rev. Lett.* 88, 25 (2002).